Anisotropic Rashba splitting dominated by out-of-plane spin polarization in two-dimensional Janus XA_2Y (A= Si, Sn, Ge; X, Y= Sb, Bi) with surface imperfection

Arif Lukmantoro and Moh. Adhib Ulil Absor
Departement of Physics, Faculty of Mathematics and Natural Sciences, Universitas Gadjah Mada, Sekip Utara BLS 21 Yogyakarta 55186 Indonesia

(Received 12 August 2023; accepted 11 October 2023; published 23 October 2023)

The anisotropic Rashba effect allows for the manipulation of electron spins in a more precise and tunable manner since the magnitude of the Rashba splitting and orientation of the spin textures can be simply controlled by tuning the direction of the externally applied electric field. Herein, we predict the emergence of the anisotropic Rashba effect in the two-dimensional (2D) Janus XA_2Y constructed from group-IV (A = Si, Sn, Ge) and group-V (X, Y = Sb, Bi) elements having trigonal prismatic structures but lacking in-plane mirror symmetry. Due to the lowering point-group symmetry of the crystal, the Rashba spin splitting is enforced to become anisotropic around certain high-symmetry points in the Brillouin zone and preserves the out-of-plane spin textures. We illustrate this behavior using density functional theory calculations supplemented with $\vec{k} \cdot \vec{p}$ analysis on the Janus $SbSi_2Bi$ monolayer as a representative example. Specifically, we observed large and anisotropic Rashba splitting with a prominent contribution of the out-of-plane spin textures in the conduction band minimum around the M point and valence band maximum around the Γ point. More importantly, the anisotropic spin splitting and out-of-plane spin polarization are sensitively affected by surface imperfections, depending on the concentration and configuration of the X and Y elements in the 2D Janus XA_2Y surface. Our paper offers the possibility to realize the present systems for spintronics applications.

DOI: 10.1103/PhysRevMaterials.7.104005

I. INTRODUCTION

The spin-orbit coupling (SOC) in crystalline solids has gained increasing significance in spintronics since it offers a way to manipulate the spin of electrons without the need for an external magnetic field [1]. Several intriguing phenomena associated with SOC have been observed, such as spin relaxation [2,3], spin Hall effect [4], spin galvanic effect [5], and spin ballistic transport [6]. In systems lacking inversion symmetry, SOC generates a momentum-dependent spin-orbit field that breaks the spin degeneracy and creates nontrivial spin textures in the spin-split bands through the Rashba [7] and Dresselhaus [8] effects. The Rashba effect has been extensively studied on systems with structural asymmetries, such as semiconductor quantum wells [9–11], surfaces of heavy metals [12,13], and various two-dimensional (2D) layered materials [14–18]. In contrast, the Dresselhaus effect occurs in systems that exhibit bulk asymmetries, including bulk zinc-blende [19] and wurtzite [20] semiconductors. In particular, the Rashba effect has garnered much attention due to its ability to create nonequilibrium spin polarizations and electrically manipulate them by simply tuning the gate voltage [11,21].

The Rashba SOC in its simplest form, which is linear in k, only produces isotropic spin splitting exhibiting concentric circles of Fermi contour lines with the in-plane chiral spin textures. However, when the anisotropy term is introduced in the Rashba SOC, the Fermi contour lines lose their circular shape and result in anisotropic spin splitting. Notably, the anisotropic Rashba effect has the potential to alter the characteristics of spin textures, such as giving rise to out-of-plane spin textures [22–26]. Such spin textures could enable field-free spin-orbit torque switching of perpendicular magnetization [27], which may impact the transport properties such as the intrinsic spin-Hall effect [28] and anomalous Hall effect [29]. On the other hand, the anisotropic Rashba SOC, having different weights of Rashba SOC strength along the different wave vector directions, may induce unusual asymmetric spin relaxation [30,31]. Under the asymmetric spin-relaxation processes, the presence of an electric current along with the Rashba SOC can induce current-induced spin polarization, which is very distinct from the spin Hall effect, known as the Rashba-Edelstein effect (REE) [32–34], which allows for the conversion between charge and spin degrees of freedom. For systems having strongly anisotropic Rasahba SOC, the largest REE occurs in the maximum accumulated spin density along the wave vector $\vec{k}$ direction with the largest Rashba SOC strength. Thus, it is possible to precisely control both the magnitude and orientation of the spin generated by the charge current by merely tuning the direction of the externally applied electric field. In addition, the anisotropic Rashba effect also significantly affects the spin Hall angle, as demonstrated by Yang *et al.* in graphene [35]. Therefore, by involving the anisotropy in the Rashba SOC and the spin textures, opportunities can be explored in the field of spintronics.

The anisotropic Rashba effect can be achieved by incorporating the interplay between the Rashba and Dresselhauss SOCs realized through the interference of structure inversion asymmetry and bulk inversion asymmetry, as

 ©2023 American Physical Society

previously demonstrated on various semiconductors quantum well [36,37]. However, due to the small of the Rashba SOC strength, efficient spin manipulation by an applied electric field is still questionable. Another approach to induce anisotropy involves reducing the crystal's symmetry, which can be accomplished through material engineering techniques such as surface reconstruction [38,39], surface atomic, or molecular absorption [40,41], and dimensional reduction to 2D structures [42–46]. The anisotropic Rashba splitting resulting from the presence of symmetry-reduced surface states has been previously reported on Au(110) [38] and W(110) [39] surfaces which possess a point-group symmetry of C_{2v}. Similarly, the absorption of a hydrogen atom on a ZnO $(10\bar{1}0)$ surface [41] and NH_3 and BH_3 molecules on a $BiAg_2$/Bi(111) surface [40], both exhibiting a point group symmetry of C_s, demonstrates the generation of anisotropic Rashba effect via surface atomic or molecular absorption. Although surface reconstruction and surface molecular absorption have advantageous characteristics, they also bring forth challenges related to surface stability [47,48]. Hence, utilizing material in the form of a 2D monolayer (ML) structure is the most suitable method to induce the anisotropic Rashba effect, which not only offers excellent stability but also provides a geometrical advantage in forming interfaces and heterostructures [49,50], which holds potential for miniaturization spintronic devices. However, to the best of our knowledge, only a few classes of the 2D ML systems have been reported to support the anisotropic Rashba effect, including black-phosphorene [42], BiTeI [44], and 2D Janus systems such as $MSi_2P_xAs_y$ (M = Mo, W) MLs [51] and transition metal dichalcogenides (TMDcs) MXY (M = W, Mo, Pt; X, Y = S, Se, Te) MLs [43,45,46,52]. Hence, the search for a 2D ML system that exhibits an anisotropic Rashba effect is greatly sought after, as it has the potential to expand the range of materials suitable for spintronics applications.

In this paper, through first-principles density-functional theory (DFT) calculations supplemented by $\vec{k}\cdot\vec{p}$-based symmetry analysis, we predict the emergence of anisotropic Rashba effect having dominant out-of-plane spin polarization in 2D Janus XA_2Y MLs constructed from a combination of group IV (A = Si, Sn, Ge) and group V (X, Y = Sb, Bi) elements. These materials possess trigonal prismatic structures but lack in-plane mirror symmetry. Previously, the stability and electronic properties of various 2D group IV and V compounds have been widely studied [53–58]. The absence of the in-plane mirror symmetry in Janus XA_2Y MLs reduces the point-group symmetry of the crystal, enforcing the Rashba SOC to become anisotropic around certain high-symmetry $\vec{k}$ points in the first Brillouin zone (FBZ) and preserves the significant out-of-plane spin textures. These properties are especially examined in the Janus $SbSi_2Bi$ ML as a representative example of the Janus XA_2Y MLs, which is notably apparent in the vicinity of the M point in the conduction band minimum (CBM) and around the Γ point in the valence band maximum (VBM). Importantly, the anisotropic spin splitting and out-of-plane spin textures are sensitively affected by surface imperfections, depending on the concentration and configuration of the X and Y elements in the 2D Janus XA_2Y MLs surface. Our results demonstrate the potential to expand the range of experimentally accessible 2D materials, thus opening avenues for their utilization in spintronics applications.

II. COMPUTATIONAL DETAILS

We have carried out DFT calculations adopting norm-conserving pseudopotentials and optimized pseudoatomic localized basis functions [59] implemented in the OPENMX code [60–62]. The generalized gradient approximation by Perdew, Burke, and Ernzerhof (GGA-PBE) [63,64] was used as the exchange-correlation functional. We used the basis functions as the linear combination of multiple pseudoatomic orbitals (PAOs) generated using a confinement scheme [61,62,65]. Here, two s-, two p-, and two d-character numerical PAOs were applied. The FBZ integration was carried out using the $12 \times 12 \times 1$ k-point mesh. To prevent artificial interactions among the periodic images generated by the periodic boundary condition, we employed a periodic slab model for the Janus XA_2Y MLs. This model included a sufficiently large vacuum layer (25 Å) in the nonperiodic direction. We optimized the lattice and positions of the atoms until the Hellmann-Feynman force components acting on each atom was less than 10^{-3} eVÅ, where the energy convergence criterion was set to 10^{-9} eV. Phonon dispersion band is used to evaluate the dynamical stability of the Janus XA_2Y MLs obtained by using ALAMODE code [66] based on the force constants obtained from the OpenMX code calculations.

The spin-vector component (S_x, S_y, S_z) of the spin polarization in the reciprocal lattice vector $\vec{k}$ was inferred by analyzing the spin-density matrix [67]. The spin-density matrix, denoted as $P_{\sigma\sigma'}(\vec{k}, \mu)$, is computed using the spinor Bloch wave function, $\Psi^{\sigma}_{\mu}(\vec{r}, \vec{k})$, through the following equation:

$$P_{\sigma\sigma'}(\vec{k}, \mu) = \int \Psi^{\sigma}_{\mu}(\vec{r}, \vec{k})\Psi^{\sigma'}_{\mu}(\vec{r}, \vec{k})d\vec{r} = \sum_{n}\sum_{i,j}[c^{*}_{\sigma\mu i}c_{\sigma'\mu j}S_{i,j}]e^{\vec{R}_n\cdot\vec{k}}, \quad (1)$$

where $\Psi^{\sigma}_{\mu}(\vec{r}, \vec{k})$ is obtained after self-consistent is achieved in the DFT calculation. In Eq. (1), S_{ij} is the overlap integral of the ith and jth localized orbitals, $c_{\sigma\mu i(j)}$ is expansion coefficient, σ (σ') is the spin index (↑ or ↓), μ is the band index, and $\vec{R}_n$ is the nth lattice vector.

In our DFT calculation, we considered the Janus XA_2Y MLs where Si, Sn, and Ge atoms are chosen as A (group IV) elements, while Sb and Bi atoms are taken as X and Y (group V) elements. These elements are chosen due to the larger atomic Z number, which is expected to induce the significant SOC. To confirm the stability of Janus XA_2Y MLs, we calculate the formation energy, E_f, by using the following relation:

$$E_f = E_{XA_2Y} - \frac{1}{n_X + n_Y + n_A}(n_X E_X + n_Y E_Y + n_A E_A), \quad (2)$$

where E_{XA_2Y} is the total energy of Janus XA_2Y MLs. E_X, E_Y, and E_A are the chemical potentials of isolated X, Y, and A atoms, respectively. n_X, n_Y, and n_A are the number of X, Y, and A atoms in the super cell or unit cell, respectively.

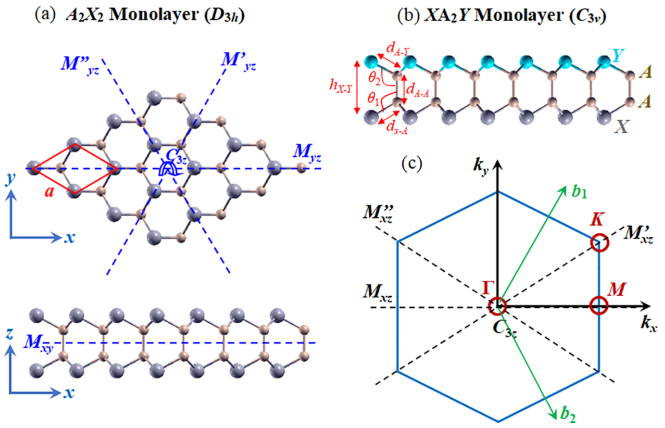

FIG. 1. Atomic structures of (a) the A_2X_2 monolayers and (b) Janus XA_2Y MLs corresponding to the first Brillouin zone (FBZ) (c) are shown. The unit cell of the crystal is indicated by the blue lines. The structural parameters including the bond length between X and A (δ_{X-A}), the bond length between Y and A atoms (δ_{Y-A}), the bond length between A atoms (δ_{A-A}), the out-of-plane distance between X and Y atoms (h_{X-Y}), and the bond angles of $X-A-A$ (θ_1) and $A-A-Y$ (θ_2) are indicated. The FBZ is characterized by the Γ, Γ, M, and K high-symmetry points. The symmetry operations in the crystal consisting of identity (E), in-plane mirror reflection (M_{xy}), out-of-plane mirror reflection (M_{xz}, M'_{xz}, M''_{xz}), and threefold rotation around the z axis (C_3, C_3^2) are shown.

III. RESULTS AND DISCUSSION

First, we discuss the structural symmetry and stability of the 2D Janus XA_2Y MLs. Previously, theoretical studies have been conducted on stable 2D systems formed by group IV and V compounds with an A_2X_2 ML structure [53–56,58], and some of these systems have been successfully synthesized [57]. These compounds consist of covalently bonded quadruple atomic layers arranged in an alternating $X-A-A-X$ sequence, resulting in a trigonal prismatic structure where A atoms form a triangular prism around the X dimer [Fig. 1(a)]. This structure is similar to that previously reported on GaSe MLs [68], which is reminiscent of the 2H phase of TMDCs MLs [69]. The A_2X_2 MLs possess crystal symmetry belonging to the $P\bar{6}m_2$ space group with a D_{3h} point group. When these MLs are transformed into Janus structures, namely, XA_2Y MLs, by substituting group-V atoms (X) on one side with different group-V atoms, the in-plane mirror symmetry M_{xy} is broken [see Fig. 1(b)], and hence the symmetry of the A_2X_2 MLs becomes C_{3v} point group. Under the C_{3v} point-group symmetry, the Janus XA_2Y MLs exhibit three types of symmetry operations that preserve the structure: identity (E), out-of-plane mirror reflection (M_{xz}, M'_{xz}, M''_{xz}), and threefold rotation around the z axis (C_3, C_3^2). The corresponding FBZ is schematically shown in Fig. 1(c).

The optimized structural-related parameters associated with Janus XA_2Y MLs are presented in Table I. It is observed that the lattice constants of Janus XA_2Y MLs decrease as the atomic number of A elements decreases. Notably, $SbSn_2Bi$ ML demonstrates the largest value of 4.65 Å, while $SbSi_2Bi$ ML exhibits the smallest value of 4.01 Å. To provide a basis for comparison, we also conducted calculations for A_2X_2 MLs and discovered that the lattice constants of Janus XA_2Y MLs are approximately the average values between A_2X_2 and A_2Y_2 MLs. Furthermore, due to the strong covalent bond between A atoms, the bond length between A atoms (δ_{A-A}) in Janus XA_2Y MLs remains largely unchanged. However, as indicated in Table I, the bond length between X (Y) and A atoms, δ_{X-A} (δ_{Y-A}), increases for Janus systems as the atomic number of the A elements increases, reflecting the trend observed in lattice constants. Additionally, the variation in the distance between X and Y atoms (h_{X-Y}) in the out-of-plane direction, as well as the bond angle of $X-A-A$ (θ_1) and $A-A-Y$ (θ_2) follows the opposite pattern as the lattice constant trends.

The stability of the 2D Janus XA_2Y MLs is confirmed by calculating the formation energy E_f. It is revealed that all the considered Janus XA_2Y MLs exhibit negative formation energy, $E_f < 0$ (see Table I), indicating that they are energetically favorable to be realized in experiments, similar to the 2D Janus $MSi_2P_xAs_y$ MLs [51] and Janus TMDCs MXY MLs [43,45,46]. In addition, the stability of the 2D Janus XA_2Y MLs is also confirmed by the calculated phonon dispersion bands shown in Fig. S1 in the Supplemental Material [70]. It is clearly seen that there are no imaginary frequencies found in the phonon dispersion bands, showing that the optimized Janus XA_2Y MLs are dynamically stable. Considering the

TABLE I. The optimized structural parameters of Janus XA_2Y MLs including in-plane lattice constant a, the bond length between X and A (δ_{X-A}), the bond length between Y and A atoms (δ_{Y-A}), the bond length between A atoms (δ_{A-A}), and the out-of-plane distance between X and Y atoms (h_{X-Y}) are shown. All the structural parameters are measured in Å. Bond angle of $X-A-A$ (θ_1) and $A-A-Y$ (θ_2) are also indicated. The formation energy is represented by E_f, which is measured in eV.

2D Janus	a (Å)	δ_{X-A} (Å)	δ_{Y-A} (Å)	δ_{A-A} (Å)	h_{X-Y} (Å)	θ_1	θ_2	E_{for} (eV)
$SbSi_2Bi$	4.01	2.63	2.68	2.35	4.96	120.43	118.35	−4.8
$SbGe_2Bi$	4.19	2.73	2.77	2.51	5.13	119.43	117.64	−4.25
$SbSn_2Bi$	4.65	2.98	3.01	2.90	5.55	116.75	115.76	−3.16
Si_2Sb_2	4.00	2.67		2.36	4.86	118.43		
Si_2Bi_2	4.13	2.72		2.35	4.95	118.62		
Ge_2Sb_2	4.13	2.71		2.51	5.10	118.44		
Ge_2Bi_2	4.27	2.80		2.51	5.16	118.24		
Sn_2Sb_2	4.37	2.98		2.89	5.71	119.16		
Sn_2Bi_2	4.51	2.97		2.87	5.72	118.62		

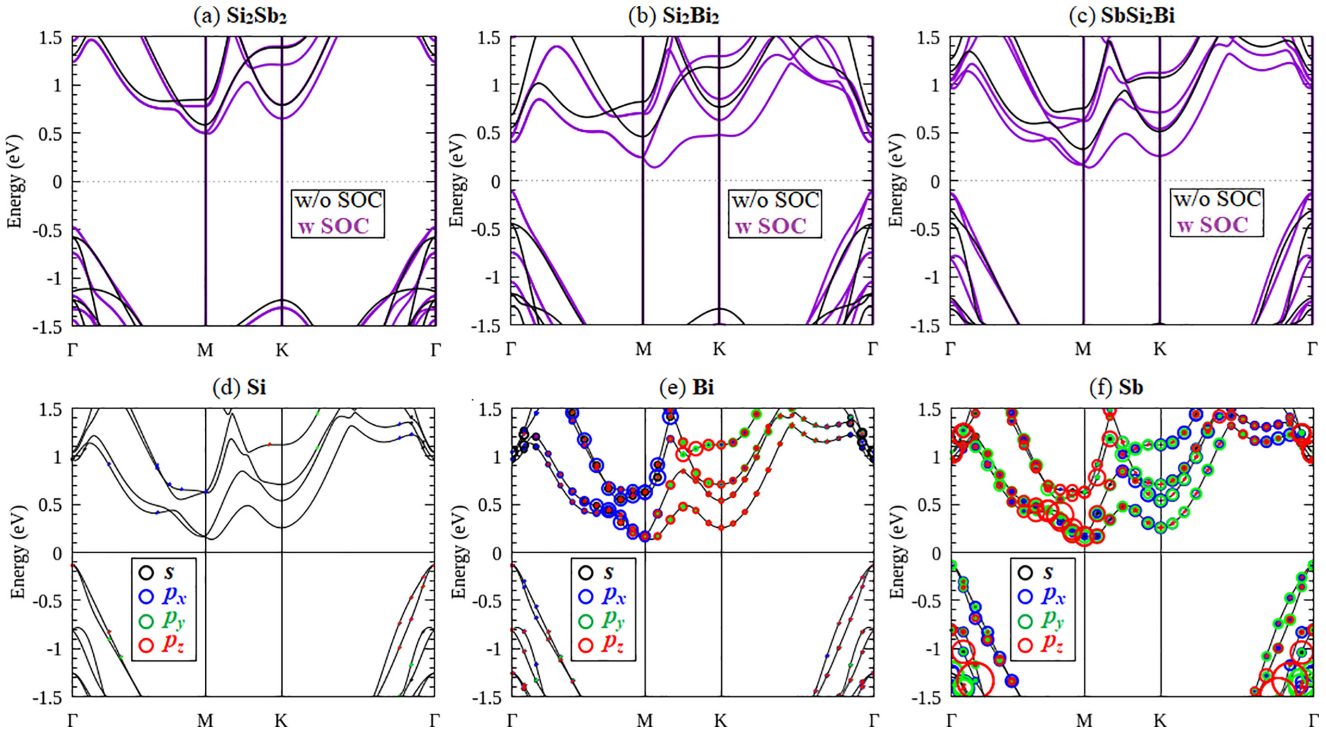

FIG. 2. Electronic band structures of (a) pure Si_2Bi_2, (b) Janus $SbSi_2Bi$, and (c) Si_2Bi_2 MLs calculated without (black lines) and with (red lines) spin-orbit coupling. Orbital-resolved electronic band structures of Janus $SbSi_2Bi$ ML calculated for (d) Si, (e) Bi, and (f) Sb atoms are presented. Here, blue, green, and red colors of circles represent s, $(p_x + p_y)$, and p_z orbitals. The radii of the circles reflect the magnitudes of spectral weight of the particular orbitals to the band.

fact that the Janus $SbSi_2Bi$ ML exhibits the lowest formation energy (see Table I), in the following discussion we will particularly focus on the Janus $SbSi_2Bi$ ML as a representative example of Janus XA_2Y MLs.

Figures 2(a)–2(c) depict the electronic band structures of the Janus $SbSi_2Bi$ ML compared to those of the pure Si_2X_2 (X = Sb, Bi) MLs. The calculations were performed both without (black lines) and with (red lines) consideration of the SOC. Similar to the pure Si_2X_2 MLs, the Janus $SbSi_2Bi$ ML exhibits an indirect band gap, where the CBM and VBM are situated at the M and Γ points, respectively. The calculated band gap of the Janus $SbSi_2Bi$ ML is 0.70 eV at the GGA-PBE level, which is smaller than that of the pure Si_2Sb_2 (0.94 eV) and Si_2Bi_2 (1.2 eV) MLs. Analysis of the band projections onto the atoms confirms that the CBM of the Janus $SbSi_2Bi$ ML predominantly arises from strong admixtures between Bi-$p_x + p_y$, Bi-p_z, Sb-$p_x + p_y$, and Sb-p_z orbitals, while the VBM is mainly contributed by the Sb-p_y and Sb-p_z orbitals [Figs. 2(d)–2(f)].

Turning the SOC, the indirect band gap of the $SbSi_2Bi$ ML remains but decreases by approximately 0.3 eV, comparable to the pure Si_2Bi_2 ML (0.25 eV) and much smaller than that of the pure Si_2Sb_2 ML (0.9 eV). Due to the absence of inversion symmetry in both the Janus $SbSi_2Bi$ ML and pure Si_2X_2 MLs, all bands exhibit spin splitting, except at high-symmetry points (Γ and M) due to time reversibility [Figs. 2(a)–2(c)]. However, for the pure Si_2X_2 MLs, the presence of in-plane mirror symmetry M_{xy} [see Fig. 1(a)] preserves the spin degeneracy of bands along the $\Gamma - M$ line [Figs. 2(a) and 2(b)]. This degeneracy is lifted in the Janus $SbSi_2Bi$ ML [Fig. 2(c)] because of the broken M_{xy} mirror symmetry [see Fig. 1(b)]. The observed spin splitting along the $\Gamma - M$ line in the Janus $SbSi_2Bi$ ML is expected to be crucial in generating spin-polarized states through the Rashba effect, which holds significance for the operation of spin-field effect transistors (SFETs) [71].

To further examine the spin-splitting characteristics within the Janus $SbSi_2Bi$ ML, our focus is directed towards the spin-split bands near the Fermi level, as depicted in Fig. 3(a). The outcomes demonstrate significant spin splitting at the CBM around the M and K points, as well as at the VBM around the Γ point [as indicated in the inset of Fig. 3(a)]. Notably, the spin splitting observed around the M and Γ points displays an anisotropic behavior, evident in the calculated spin-splitting energy mapped across the entire FBZ region, as shown in Figs. 3(b) and 3(c). In this regard, the spin-splitting energy exhibits maximum values along the $M - K$ line and minimum values along the $\Gamma - M$ line, both in the CBM and VBM. For instance, at the CBM, the most significant spin splitting, up to 0.65 eV, occurs at the k point along the $M - K$ line, whereas only 0.1 eV is observed at the k point along the $\Gamma - M$ line [Fig. 3(b)]. In particularly, a substantial spin splitting of 0.52 eV has been identified at the non-time-reversal invariant K point in the CBM, which is notably larger than that observed in various 2D Janus MLs (0.14–0.48 eV) [43,45,46,51]. The considerable magnitude of spin splitting observed in these present systems signifies their potential for spintronics functionality, operating even at room temperature [72].

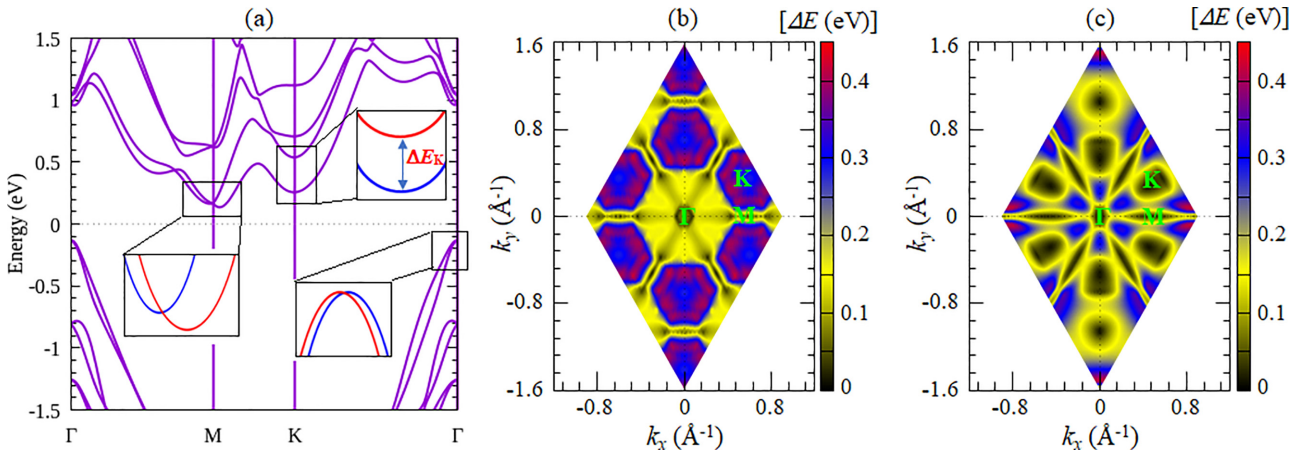

FIG. 3. (a) The highlighted spin-split bands of the Janus $SbSi_2Bi$ ML near the Fermi level around M and K points at the CBM and Γ point at the VBM. (b), (c) Spin-splitting energy of the Janus $SbSi_2Bi$ monolayer mapped in the first Brillouin zone for CBM and VBM, respectively, are shown. The magnitude of the spin-splitting energy, ΔE, defined as $\Delta E = |E(k,\uparrow) - E(k,\downarrow)|$, where $E(k,\uparrow)$ and $E(k,\downarrow)$ are the energy bands with up spin and down spin, respectively, is represented by the color scales.

To further analyze the Rashba anisotropy observed in the Janus $SbSi_2Bi$ ML, we present in Figs. 4(a)–4(c) the expectation values of spin components (S_x, S_y, S_z) projected onto the spin-split bands near the Fermi level. Our findings reveal that, in addition to the in-plane spin components (S_x, S_y) observed in the spin-split polarized states at the k point along the $\Gamma - M$ line, a significant contribution of the out-of-plane spin component (S_z) is identified in the spin-split polarized states at the k point along the $M - K - \Gamma$ line. This anisotropy of the spin polarization direction in k space within the Janus $SbSi_2Bi$ ML is most clearly illustrated in Figs. 4(d) and 4(e) by the spin textures projected onto the FBZ around the M and Γ points in the CBM and VBM, respectively. In these figures, for clarity, we indicate the direction of the in-plane spin polarization using arrows, while the out-of-plane spin polarization is represented by colors. Around the M point, the spin textures exhibit a C_s symmetry of spin polarization, characterized by the reversal of the out-of-plane spin polarization mirrored at $k_x = 0$ [Fig. 4(d)]. Conversely, around the Γ point in the VBM, the spin textures display a C_{3v} symmetry of spin polarization, characterized by the in-plane spin polarization and threefold pattern of the out-of-plane spin orientation [Fig. 4(d)]. These particular spin textures observed around the M and Γ points deviate from the conventional Rashba spin textures commonly observed in semiconductor quantum wells [9–11], surfaces of heavy metals [12,13], and various 2D layered materials [14–18]. Notably, the anisotropy in the spin-polarization direction, with a prominent out-of-plane spin polarization component, can impede electron back-scattering in spin transport and induce long-lived helical spin-wave modes by suppressing the spin relaxation [73]. This unique feature holds great promise for efficient spintronics applications.

To understand the origin of the anisotropic of the spin splitting and spin polarization direction, we developed a $\vec{k} \cdot \vec{p}$ model based on the symmetry analysis. The band dispersion around the high-symmetry point can be determined by the Hamiltonian $H(k)$ allowed by symmetry, so $H(\vec{k}) = O^{\dagger}H(\vec{k})O$, where O represents symmetry operations associated with the wave vector group (G) corresponding to the high-symmetry point and time-reversal symmetry (T). The invariant $H(k)$ should obtain the following condition [74]:

$$H_G(\vec{k}) = D(O)H(O^{-1}\vec{k})D^{-1}(O), \quad \forall O \in G, T, \tag{3}$$

where $D(O)$ is the matrix representation of operation O belonging to the point group of the wave vector G. For our Janus systems, we focus on the high-symmetry point of the FBZ depicted in Fig. 1(c), and the corresponding little group of the wave vector is outlined in Table II. The corresponding transformations of k and $\vec{\sigma}$ for all symmetry-allowed terms are listed in Table III.

First, we derive an effective $\vec{k} \cdot \vec{p}$ Hamiltonian around the high-symmetry M point. Here, the little point group of the wave vector belongs to the C_s point group (see Table II). This point group comprises mirror planes M_{xz} in addition to the identity operation E. Consequently, both the wave vector $\vec{k}$ and the spin vector $\vec{\sigma}$ can be transformed according to the symmetry operation in the C_s point group and time-reversal symmetry T. By collecting all terms that invariant under the symmetry operations of the C_s point group (Table III), the following effective Hamiltonian for the $(k_x - k_y)$ plane holds [75]:

$$H_M(k) = H_0(k) + \alpha k_x \sigma_y + \alpha' k_y \sigma_x + \alpha'' k_y \sigma_z, \tag{4}$$

where $H_0(k)$ is the part of Hamiltonian describing the nearly free-electron or -hole band dispersion written as

$$H_0(k) = E_0(k) + \delta_1 k_x^2 + \delta_2 k_y^2, \tag{5}$$

where δ_1 and δ_2 are related to the effective masses (m_x^*, m_x^*) by the relations $|\delta_1| = \hbar^2/2m_x^*$ and $|\delta_2| = \hbar^2/2m_y^*$, respectively. $\vec{\sigma}$ are the Pauli matrices describing spin degrees of freedom, while α, α', and α'' are the SOC parameters.

Solving the eigenvalue problem involving the Hamiltonian of Eq. (4), we obtain the following energy band dispersion:

$$E_M(k) = E_0(k) + \delta_1 k_x^2 + \delta_2 k_y^2 + \pm\sqrt{\alpha^2 k_x^2 + (\alpha'^2 + \alpha''^2)k_y^2}. \tag{6}$$

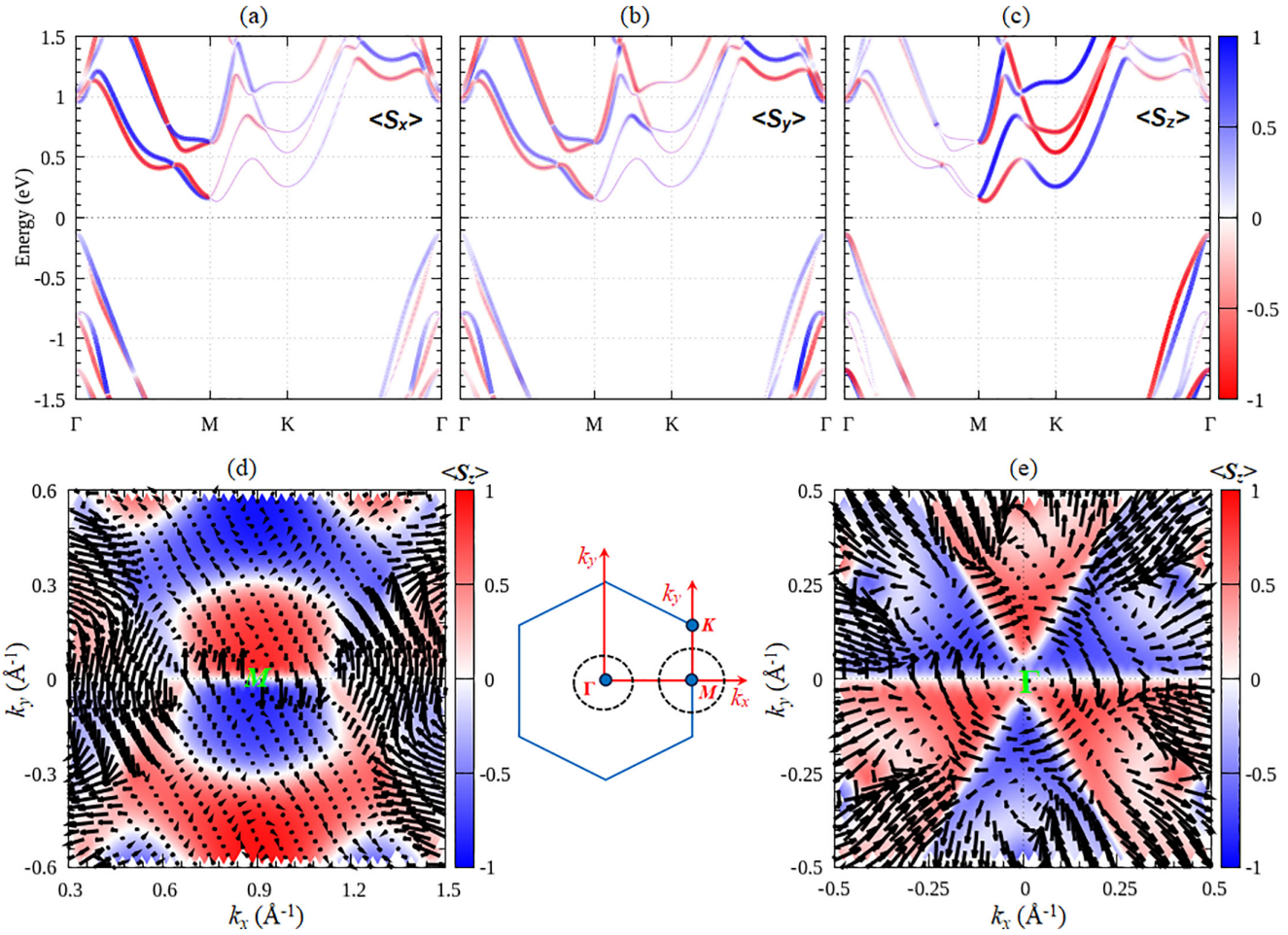

FIG. 4. Spin-resolved projected to the bands of Janus $SbSi_2Bi$ monolayer for (a) S_x, (b) S_y, and (c) S_z spin components of spin polarization $\vec{S}$ is shown. The spin textures mapped in the FBZ calculated for the bands around (d) M and (e) Γ points are shown. The arrows represent the magnitude of the in-plane spin spin components (S_x, S_y), while the color represents the out-of-plane spin component (S_z). The insets show the position of the M and Γ points in the FBZ used in the spin-texture calculations.

The corresponding eigenstates are given as

$$\psi_k^{\pm} = \frac{e^{i\vec{k}\cdot\vec{r}}}{\sqrt{2\pi(\rho_{\pm}^2+1)}}\begin{pmatrix}\frac{i\alpha k_x-\alpha' k_y}{\alpha'' k_y \mp\sqrt{\alpha^2k_x^2+(\alpha'^2+\alpha''^2)k_y^2}}\\ 1\end{pmatrix}, \quad (7)$$

where $\rho_{\pm} = \frac{\alpha^2k_x^2+\alpha'^2k_y^2}{(\alpha'' k_y \mp\sqrt{\alpha^2k_x^2+(\alpha'^2+\alpha''^2)k_y^2})^2}$. The expectation value of the spin operator is obtained from $\vec{s}^{\pm} = \frac{1}{2}\langle\psi_k^{\pm}|\vec{\sigma}|\psi_k^{\pm}\rangle$, resulting in

$$(S_x, S_y, S_z)^{\pm} = \pm\frac{1}{2\sqrt{\alpha^2k_x^2+(\alpha'^2+\alpha''^2)k_y^2}}(\alpha' k_y, \alpha k_x, \alpha'' k_y). \quad (8)$$

As evident from Eq. (6) that the anisotropic Rashba spin splitting is achieved depending on the magnitude of the SOC parameter in the spin-split bands along the k_x ($M-\Gamma$) direction, $\alpha^{M-\Gamma} = \alpha$, and along the k_y ($M-K$) direction, $\alpha^{M-K} = \sqrt{\alpha'^2+\alpha''^2}$. By fitting the DFT band dispersion of Fig. 3(a) along the $M-\Gamma$ and $M-K$ directions with Eq. (6), we find that $\alpha^{M-\Gamma} = 0.08$ eVÅ and $\alpha^{M-K} = 1.34$ eVÅ. Since $\alpha^{M-\Gamma} \ll \alpha^{M-K}$, the Rashba splitting exhibits a high degree of anisotropy, which is consistent with the spin-splitting energy shown in Fig. 3(b). Moreover, from Eq. (8), we can estimate the ratio between α' and α'' by comparing the in-plane and out-of-plane spin component along the $M-\Gamma$ direction, and found that $\alpha'/\alpha'' = 0.024$. Therefore, by using $\alpha^{M-K} = \sqrt{\alpha'^2+\alpha''^2} = 1.34$, we find that $\alpha' = 0.032$ eVÅ and $\alpha'' = 1.33$ eVÅ. The larger value of α'' indicates that the spin-split states around the M point are dominated by the out-of-plane

TABLE II. The little point group of the wave vector $\vec{k}$ in the high-symmetry points and lines in the FBZ for Janus XA_2Y MLs. The symmetry operations occurring in the high symmetry points and lines in the FBZ are indicated in Fig. 1(c).

$\vec{k}$ point or line	Janus XA_2Y (C_{3v})	symmetry operations
Γ	C_{3v}	E, $(M_{xz}, M'_{xz}, M''_{xz})$, (C_3, C_3^2)
M	C_s	E, M_{xz}
K	C_3	E, (C_3, C_3^2)
$\Gamma-M$	C_s	E, M_{xz}
$\Gamma-K$	C_1	E
$M-K$	C_1	E

TABLE III. The transformations of $(\sigma_x, \sigma_y, \sigma_z)$ and (k_x, k_y) with respect to the generators of C_{3v}, C_s, and C_1 point groups and time-reversal operator (T). Note that only these generators along with time-reversal $T = i\sigma_y K$ operation, where K is complex-conjugation operator, are considered to construct the $\vec{k} \cdot \vec{p}$ model. The last column shows the terms which are invariant under point-group operation.

Operations	(k_x, k_y)	$(\sigma_x, \sigma_y, \sigma_z)$	Invariant terms
$C_{3z} = e^{-i\pi/3\sigma_z}$	$\frac{1}{2}([-k_x + \sqrt{3}k_y], [-\sqrt{3}k_x - k_y])$	$(\frac{1}{2}[-\sigma_x + \sqrt{3}\sigma_y], \frac{1}{2}[-\sqrt{3}\sigma_x - \sigma_y], \sigma_z)$	$k_x\sigma_y - k_y\sigma_x$, $k_y(3k_x^2 - k_y^2)\sigma_z$, $k_x(k_x^2 - 3k_y^2)\sigma_z$
$M_{xz} = i\sigma_y$	$(k_x, -k_y)$	$(-\sigma_x, \sigma_y, -\sigma_z)$	$k_i^m k_y\sigma_x$, $k_i^m k_y\sigma_z$, $k_i^m k_x\sigma_y$ $(i = x, y; m = 0, 2)$
$T = i\sigma_y K$	$(-k_x, -k_y)$	$(-\sigma_x, -\sigma_y, -\sigma_z)$	$k_i\sigma_j$ $(i = x, y; j = x, y, z)$

spin component, which also agrees well with the calculated spin textures shown in Fig. 4(d).

Next, we discuss the origin of the anisotropic Rashba splitting around the Γ point. The little point group of the wave vector associated with the Γ point is C_{3v}, comprising trivial identity operation (E), threefold rotation C_{3z}, and three mirror planes $(M_{xz}, M'_{xz}, M''_{xz})$ (see Table II). The effective $\vec{k} \cdot \vec{p}$ Hamiltonian for the $(k_x - k_y)$ plane taking into account the symmetry invariants up to cubic in k (see Table III) can be expressed as [75]

$$H_\Gamma(k) = H_0(k) + \alpha(k_y\sigma_x - k_x\sigma_y) + \beta\big[\big(k_y^3 + k_y k_x^2\big)\sigma_x - \big(k_y{}^2 k_x + k_x{}^3\big)\sigma_y\big] + \gamma\big(k_y{}^3 - 3\big(k_y k_x^2\big)\big)\sigma_z, \quad (9)$$

where α is the linear term of the SOC parameter, while β and γ are the cubic terms of the SOC parameters. By defining $k = \sqrt{k_x{}^2 + k_y{}^2}$ and $\phi = \arccos(k_x/k)$, where ϕ is the azimuthal angle of momentum k with respect to the x axis along the $\Gamma - M$ direction in the FBZ, we obtained that the Hamiltonian of Eq. (9) can be written as

$$H_\Gamma(k) = H_0(k) + (\alpha k + \beta k^3)(\sin(\phi)\sigma_x - \cos(\phi)\sigma_y) + \gamma k^3 \sin(3\phi)\sigma_z. \quad (10)$$

The energy eigenvalues of Eq. (10) are given as

$$E_\Gamma(k) = E_0(k) + \delta_1 k_x^2 + \delta_2 k_y^2 + \pm\sqrt{(\alpha k + \beta k^3)^2 + \gamma^2 k^6 \sin^2(3\phi)}. \quad (11)$$

We emphasized here that the second and third terms of $H_\Gamma(k)$ in Eq. (10), respectively, will induce in-plane and out-of-plane spin polarization, so the spin polarization at fixed energy is given by

$$(S_x, S_y, S_z)^\pm = [\pm(\alpha k + \beta k^3)\sin(\phi), \mp(\alpha k + \beta k^3)\cos(\phi), \mp\gamma k^3 \sin(3\phi)], \quad (12)$$

which is in agreement with the spin textures plots in Fig. 4(e). As demonstrated in Eq. (11), the anisotropic Rashba spin splitting near the Γ point is controlled by distinct parameters: α, β, and γ, which vary based on the chosen k path along the $\Gamma - M$ and $\Gamma - K$ orientations. Our fitting analysis of the spin-split bands illustrated in Fig. 3(a) at the VBM, both along the $\Gamma - M$ and $\Gamma - K$ directions, utilizing Eq. (11), revealed the computed values for the SOC parameters: $\alpha^{\Gamma-M} = 0.74$ eVÅ, $\alpha^{\Gamma-K} = 0.88$ eVÅ, $\beta^{\Gamma-M} = 52.8$ eVÅ^3, $\beta^{\Gamma-K} = 37.8$ eVÅ^3, and $\gamma^{\Gamma-K} = 0.9$ eVÅ^3. It's important to highlight that our fitting analysis of the spin-split bands along the $\Gamma - M$ direction yielded $\alpha^{\Gamma-M} = 0$, as a result of the vanishing term $\gamma^2 k^6 \sin^2(3\phi)$ in Eq. (11) when the k path is chosen along the $\Gamma - M$ direction. Consequently, the out-of-plane spin polarization S_z along the $\Gamma - M$ direction becomes zero. This finding is consistent with the spin-resolved projected bands depicted in Figs. 4(a)–4(c) and the spin textures shown in Fig. 4(e).

We summarize the anisotropic Rashba parameters of the 2D Janus XA_2Y MLs around the M and Γ points in the CBM and VBM, respectively, in Table IV and compare the result with a few selected 2D materials supporting anisotropic Rashba splitting from previously reported data. In particular, the magnitude of the linear terms $(\alpha^{M-\Gamma}, \alpha^{M-K}, \alpha^{\Gamma-M}, \alpha^{\Gamma-K})$ of the SOC parameters are much larger than that observed on black-phosphorene [42] and 2D Janus $MSi_2P_xAs_y$ MLs [51], and 2D Janus TMDCs MLs including $MSSe$ Mls [43], MXY MLs [46], and PtXY MLs [45], and are comparable with that observed on BiTeI ML [44]. Notably, the magnitudes of these SOC parameters increase as the Janus XA_2Y MLs become heavier. For instance, the α^{M-K} value around the M point in the Janus $SbSn_2Bi$ ML (1.6 eVÅ) far exceeds that of the Janus $SbSi_2Bi$ ML (1.34 eVÅ), as shown in Table IV. To enhance the spin splitting magnitude in these materials, it's possible to introduce heavier elements with strong SOC through doping [76] and apply strain [77,78], making the experimental detection of this phenomenon is more feasible, particularly utilizing techniques like spin-resolved photoemission spectroscopy.

We have discovered that the Janus XA_2Y MLs exhibit large and anisotropic Rashba splitting, suggesting their potential utility in spintronics applications. Nonetheless, the creation of these Janus XA_2Y MLs is expected to be sensitive to surface imperfections, akin to what has been observed in previous Janus TMDCs MLs. In typical TMDCs, the Janus arrangement is achieved through techniques involving sulfurization [79,80] and selenization [81], where one plane of the ML surface consists of different chalcogen atoms. Moreover, recent experimental work has demonstrated notable advancements in controlling the chalcogen exchange processes [79–84], enabling the formation of the surface imperfection through selective modification of only a fraction of the chalcogen atoms

TABLE IV. Several selected 2D materials systems supporting the anisotropic Rashba splitting. The SOC parameters are shown, including the linear terms [$\alpha^{M-\Gamma}$, α^{M-K} (in eVÅ)] of the SOC parameters around the M point in the CBM and the linear terms [$\alpha^{\Gamma-M}$, $\alpha^{\Gamma-K}$ (in eVÅ)] and cubic terms [$\beta^{\Gamma-M}$, $\beta^{\Gamma-K}$, $\gamma^{\Gamma-M}$, $\gamma^{\Gamma-K}$ (all in eVÅ^3)] of the SOC parameters around the Γ point in the VBM.

2D Materials	HSP	$\alpha^{\Gamma-M}$ ($\alpha^{M-\Gamma}$)	$\alpha^{\Gamma-K}$ (α^{M-K})	$\beta^{\Gamma-M}$	$\beta^{\Gamma-K}$	$\gamma^{\Gamma-M}$	$\gamma^{\Gamma-K}$	Ref.
$SbSi_2Bi$	Γ (M)	0.74 (0.08)	0.88 (1.34)	52.8	37.8	0.0	0.9	This paper
$SbGe_2Bi$	Γ (M)	1.45 (0.27)	1.82 (1.45)	63.9	91.3	0.0	−1.22	This paper
$SbSn_2Bi$	Γ (M)	1.53 (0.29)	1.95 (1.6)	−212.8	−280.1	0.0	108.3	This paper
BP	Γ	0.0109	0.0036					Ref. [42]
MSSe (M = Mo,W)	Γ		0.004–0.17					Ref. [43]
MoXY (X, Y = S,Se, Te)	Γ	0.077–0.479	0.77–0.487					Ref. [46]
WXY (X, Y = S,Se, Te)	Γ	0.157–0.524	0.158–0.514					Ref. [46]
PtXY (X, Y = S,Se, Te)	Γ	0.435–1.654	0.746–1.333					Ref. [45]
MSi$_2$P$_x$As$_y$ (M = W, Mo)	Γ	0.0–0.6	0.073–2.77					Ref. [51]
BiTeI	Γ	1.82						Ref. [44]

in one of the surface layers of TMDCs MLs. By employing a similar principle, it is also feasible to create Janus XA_2Y MLs through surface imperfections by partially substituting the group-V (X, Y) atoms in one of the surface layers of pure A_2X_2 (A_2Y_2) MLs. Recently, 2D monoelemental (Bi and Sb) MLs with a buckled honeycomb lattice structure containing two layers have been successfully synthesized experimentally [85,86]. Hence, there exists an opportunity to experimentally synthesize MLs containing ABi (ASb) by substituting the Bi (Sb) layer on one side with an A (Si, Ge, Sn) layer. Assuming successful experimental synthesis of SiBi MLs, it becomes feasible to connect two SiBi MLs in a Bi-Si-Si-Bi configuration, potentially leading to the creation of a pure Si_2Bi_2 ML comprising four atomic layers. The surface imperfection of the Si_2Bi_2 ML can be further achieved by interstitially substituting the Sb atom in the Bi site within one of the surface layers. The fully Janus $SbSi_2Bi$ ML structure can be realized when all the Bi site atoms in one of the surface layers are completely replaced by Sb atoms. Indeed, the favorable formation of the complete Janus $SbSi_2Bi$ ML is confirmed by the reduced formation energy as the Sb concentration increases, as shown in Table S1 in the Supplemental Material [70]. We would like to note that the formation of the Janus $SbSi_2Bi$ ML is more favorable when achieved through the surface imperfection of the Si_2Sb_2 ML due to the lower formation energy; see Table S1 in the Supplemental Material [70].

To ensue discussion aiming to explore the pivotal role of the surface imperfections in influencing the spin-splitting characteristics of Janus XA_2Y MLs, we show in Fig. 5 the relation between crystal symmetry, spin-split bands, and spin textures around the Γ point at the VBM of the Si_2Bi_2 ML under different concentration of the Sb substitutions. The Sb atom concentration (n_{Sb}) is expressed as a percentage relative to the number of Bi atoms on the upper surface within the framework of the 4 x 4 x 1 supercell of the Si_2Bi_2 ML. When $n_{Sb} = 0\%$, representing the pure Si_2Bi_2 ML, the crystal's D_{3h} point-group symmetry [Fig. 5(a)] enforces the appearance of the spin splitting in the electronic bands, except for k bands along the $\Gamma - M$ line [Fig. 5(b)], leading to a fully out-of-plane spin polarization with a threefold pattern [Fig. 5(c)]. With the introduction of a single Sb atom interstitially replacing the Bi atom within one of the surface layer of the Si_2Bi_2 ML ($n_{Sb} = 6.25\%$) [see Fig. 5(d)], the in-plane mirror symmetry M_{xy} is broken, resulting in the crystal's C_{3v} point group symmetry. This change lifts the spin degeneracy of the bands along the $\Gamma - M$ line [Fig. 5(e)], giving rise to a threefold pattern in both in-plane and out-of-plane spin polarization [Fig. 5(f)]. Interestingly, as the Sb concentration is increased to $n_{Sb} = 25\%$ [Fig. 5(g)], the in-plane mirror symmetry M_{xy} and the threefold rotation symmetry C_{3z} are both disrupted, yielding a stable configuration with C_s point-group symmetry. Consequently, the spin-splitting bands exhibit pronounced anisotropy [Fig. 5(h)], showcasing a reverse pattern of out-of-plane spin polarization mirrored at $k_x = 0$. Finally, with a Sb substitution of $n_{Sb} = 100\%$, the Janus $SbSi_2Bi$ ML forms [Fig. 5(j)], featuring the crystal's C_{3v} point group symmetry. This configuration shares the spin-split band and spin polarization characteristics seen in the $n = 6.25\%$ scenario but with a notably higher spin splitting energy [Figs. 5(k)–5(l)].

The impact of Sb atom substitution on the spin-splitting characteristics of the Si_2Bi_2 ML is further quantified by evaluating the SOC parameters through the application of a symmetry-adapted SOC Hamiltonian for the D_{3h}, C_{3v}, and C_s point groups; see the Supplemental Material for the explicit form of the $\vec{k} \cdot \vec{p}$ model [70]. The computed results for these SOC parameters are detailed in Table V. Notably, the linear terms of the SOC parameters experience significant enhancement with the progressive substitution of Sb atoms. This suggests that the partial substitutions of the group V (X, Y) atoms on the pure A_2X_2 (A_2Y_2) MLs offer an effective means to adjust the spin-splitting characteristics of Janus XA_2Y MLs. Thus, our discoveries highlight the potential spintronic capabilities of Janus XA_2Y MLs, with experimental realization becoming feasible.

Before closing, we would like to discuss the potential application of the current system in spintronics devices, specifically SFETs [71]. In SFETs, the response of the Rashba parameter to the external electric field, measured as the electric field response rate of the Rashba parameter denoted as $|\Delta\alpha/\Delta|\vec{E}||$, plays a crucial role in their operation. In fact, the strong response of the Rashba parameter to the external electric field has been previously reported on Bi-doped ZnO nanowires [87]. To maintain spin coherence in SFETs, it is essential to have a large Rashba parameter and a strong response to the applied electric field, as this helps reduce the length of the spin channel. By examining the Rashba parameter of

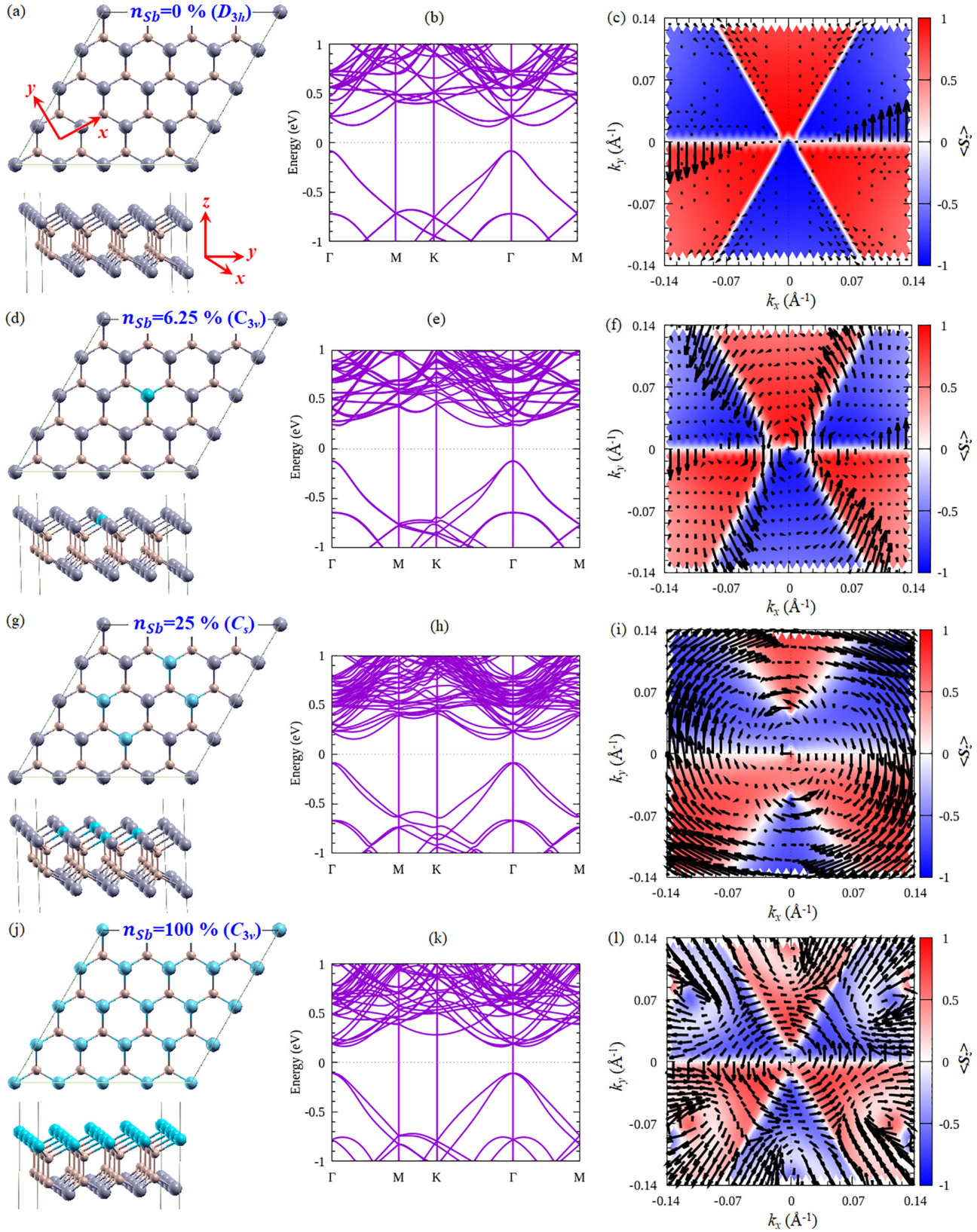

FIG. 5. The crystal structure in the top and side views, spin-split bands, and spin textures for Si_2Bi_2 ML supercell with surface imperfection are shown for (a)–(c) the clean system and doping systems with (d)–(f) Sb concentration $n_{Sb} = 6.25\%$, (g)–(i) with Sb concentration $n_{Sb} = 25\%$, and (j)–(l) Sb concentration $n_{Sb} = 100\%$.

TABLE V. The dependence of the SOC parameters on the concentration and configuration of the Sb atom on the top surface of Si_2Bi_2 ML modeled by $4 \times 4 \times 1$ supercell. The Sb atom concentration (n_{Sb}) is expressed as a percentage relative to the number of Bi atoms on the upper surface within the framework of the $4 \times 4 \times 1$ supercell. Concentration of $n_{Sb} = 0\%$ means that the system is pure Si_2Bi_2 ML, while the concentration of $n_{Sb} = 100\%$ indicates that the system forms the Janus structure of $SbSi_2Bi$ ML. The SOC parameters including the linear terms [$\alpha^{\Gamma-M}$, $\alpha^{\Gamma-K}$ (all in eVÅ)] and cubic terms [$\beta^{\Gamma-M}$, $\beta^{\Gamma-K}$, $\gamma^{\Gamma-M}$, $\gamma^{\Gamma-K}$ (all in eVÅ^3)] of the SOC parameters are shown for the VBM around the Γ point.

Concentration (%)	PGS	HSP	$\alpha^{\Gamma-M}$	$\alpha^{\Gamma-K}$	$\beta^{\Gamma-M}$	$\beta^{\Gamma-K}$	$\gamma^{\Gamma-M}$	$\gamma^{\Gamma-K}$
0	D_{3h}	Γ						0.32
6.25	C_{3v}	Γ	0.09	0.01	−70.0	79.9	0.0	0.4
12.5	C_s	Γ	0.11	0.17				
25	C_s	Γ	0.34	0.37				
50	C_s	Γ	0.21	0.36				
75	C_s	Γ	0.25	0.42				
100	C_{3v}	Γ	0.74	0.88	52.8	52.8	0.0	0.9

the Janus $SbSi_2Bi$ ML near the Γ point at the VBM, we have revealed that it exhibits a notably linear response to the electric field, as depicted in Fig. S2 of the Supplemental Material [70]. This response results in a significant response rate $|\Delta\alpha/\Delta|\vec{E}||$ of up to 0.59 eÅ^2 and 0.44 eÅ^2 along the $\Gamma - K$ and $\Gamma - M$ directions, respectively. These response rates are comparable to that reported previously on typical 2D Rashba systems including BiSb (0.92 eÅ^2) [88], T-RbPbX_3 (X = Br, I) (0.177–0.544 eÅ^2) [89], and TlSnX_3 (X = Br, I) (0.23–0.79 eÅ^2) [90]. Considering the Janus $SbSi_2Bi$ ML as the quasi-one-dimensional channel of the SFET, electron spins can undergo precession due to the Rashba effect, characterized by the precession angle $\theta = 2\alpha m^* L/\hbar^2$, where L represents the channel length of the SFET [70]. By adjusting the gate voltage of the SFET, we can manipulate the Rashba parameter α, thereby controlling the precession angle θ. Thanks to the substantially large $|\Delta\alpha/\Delta|\vec{E}||$ exhibited by the $SbSi_2Bi$ ML, we have found that the estimated channel length L is approximately 159 nm [70]). This length is comparable to the spin channel length of other primitive systems for SFETs such as BiSb (L = 158 nm) [88], T-RbPbX_3 (X = Br, I), (L = 72 − 172 nm) [89], and TlSnX_3 (X = Br, I) (L = 102 − 220 nm) [90], but is significantly smaller than the typical values of conventional SFETs ($L \approx 2 - 5$ μm) operating at room temperature [91–93]. Remarkably, the Janus XA_2Y ML with large Rashba parameters and strong electric field response rates could serve as promising candidates for SFETs.

IV. CONCLUSION

In summary, we employed first-principles DFT calculations coupled with $\vec{k} \cdot \vec{p}$-based symmetry analysis to systematically explore the properties related to SOC in the 2D Janus XA_2Y ML composed of group IV and V compounds. The absence of in-plane mirror symmetry in these Janus XA_2Y MLs reduces the crystal's point-group symmetry, causing the Rashba SOC to exhibit anisotropy around specific high-symmetry $\vec{k}$ points within the FBZ. This anisotropy also maintains pronounced out-of-plane spin patterns. We have focused our examination on the Janus $SbSi_2Bi$ ML as a representative case, where these properties are particularly noticeable near the CBM around the M point and the VBM around Γ point. Additionally, our investigation uncovered that the anisotropic spin splitting and out-of-plane spin patterns are notably influenced by surface imperfections. This dependence on imperfection characteristics encompasses the composition and configuration of X and Y elements within the 2D Janus XA_2Y MLs.

Considering the anisotropic Rashba phenomenon observed in our study, characterized by predominant out-of-plane spin polarization, it is reasonable to anticipate that this effect can be replicated in other 2D materials possessing a trigonal prismatic structure. The asymmetry in the in-plane mirror operation M_{xy} is solely responsible for driving this phenomenon. Our symmetry analysis has elucidated that various 2D systems exhibit the potential for hosting the anisotropic Rashba effect with predominant out-of-plane spin polarization. These systems include 2D Janus structures of group V-IV-III-VI MLs [94], MLs of group III-V compounds [95], and 2D Janus group III monochalcogenides MLs with oxygenation [96]. As a result, our projections are anticipated to stimulate further exploration through theoretical and experimental investigations, aiming to discover 2D materials that support the anisotropic Rashba effect. Such discoveries hold promise for advancing spintronic applications in the future.

ACKNOWLEDGMENTS

This work was supported by the Rekognisi Tugas Akhir (RTA) program (No. 5075/UN1.P.II/Dit-Lit/PT.01.01/2023), supported by Gadjah Mada University, Indonesia. A.L. thanks the Indonesian Endowment Fund for Education (LPDP) Indonesia for financial support through the LPDP scholarship program. The computation in this research was performed using the computer facilities at Gadjah Mada University, Indonesia.

[1] A. Manchon, H. C. Koo, J. Nitta, S. M. Frolov, and R. A. Duine, New perspectives for Rashba spin-orbit coupling, Nat. Mater. **14**, 871 (2015).

[2] J. Fabian and S. D. Sarma, Spin relaxation of conduction electrons, J. Vac. Sci. Technol. B **17**, 1708 (1999).

[3] N. S. Averkiev and L. E. Golub, Giant spin relaxation anisotropy in zinc-blende heterostructures, Phys. Rev. B **60**, 15582 (1999).
[4] X.-L. Qi, Y.-S. Wu, and S.-C. Zhang, Topological quantization of the spin Hall effect in two-dimensional paramagnetic semiconductors, Phys. Rev. B **74**, 085308 (2006).
[5] S. D. Ganichev, E. L. Ivchenko, V. V. Bel'kov, S. A. Tarasenko, M. Sollinger, D. Weiss, W. Wegscheider, and W. Prettl, Spin-galvanic effect, Nature (London) **417**, 153 (2002).
[6] J. P. Lu, J. B. Yau, S. P. Shukla, M. Shayegan, L. Wissinger, U. Rössler, and R. Winkler, Tunable spin-splitting and spin-resolved ballistic transport in GaAs/AlGaAs two-dimensional holes, Phys. Rev. Lett. **81**, 1282 (1998).
[7] E. Rashba, Properties of semiconductors with an extremum loop. 1. Cyclotron and combinational resonance in a magnetic field perpendicular to the plane of the loop, Sov. Phys. Solid State **2**, 1109 (1960).
[8] G. Dresselhaus, Spin-orbit coupling effects in zinc blende structures, Phys. Rev. **100**, 580 (1955).
[9] D. Stein, K. v. Klitzing, and G. Weimann, Electron spin resonance on $GaAs - Al_xGa_{1-x}As$ heterostructures, Phys. Rev. Lett. **51**, 130 (1983).
[10] L. W. van Heeringen, A. McCollam, G. A. de Wijs, and A. Fasolino, Theoretical models of Rashba spin splitting in asymmetric $SrTiO_3$-based heterostructures, Phys. Rev. B **95**, 155134 (2017).
[11] J. Nitta, T. Akazaki, H. Takayanagi, and T. Enoki, Gate control of spin-orbit interaction in an inverted $In_{0.53}Ga_{0.47}As/In_{0.52}Al_{0.48}As$ heterostructure, Phys. Rev. Lett. **78**, 1335 (1997).
[12] S.-J. Gong, C.-G. Duan, Y. Zhu, Z.-Q. Zhu, and J.-H. Chu, Controlling Rashba spin splitting in Au(111) surface states through electric field, Phys. Rev. B **87**, 035403 (2013).
[13] A. Varykhalov, D. Marchenko, M. R. Scholz, E. D. L. Rienks, T. K. Kim, G. Bihlmayer, J. Sánchez-Barriga, and O. Rader, Ir(111) surface state with giant Rashba splitting persists under graphene in air, Phys. Rev. Lett. **108**, 066804 (2012).
[14] S. Singh and A. H. Romero, Giant tunable Rashba spin splitting in a two-dimensional BiSb monolayer and in BiSb/AlN heterostructures, Phys. Rev. B **95**, 165444 (2017).
[15] M. A. U. Absor, I. Santoso, Harsojo, K. Abraha, H. Kotaka, F. Ishii, and M. Saito, Strong Rashba effect in the localized impurity states of halogen-doped monolayer $PtSe_2$, Phys. Rev. B **97**, 205138 (2018).
[16] M. D. Umar, L. D. Falihin, A. Lukmantoro, Harsojo, and M. A. U. Absor, Emergence of Rashba spin valley state in two-dimensional strained bismuth oxychalcogenides Bi_2O_2Se, Phys. Rev. B **108**, 035109 (2023).
[17] Y. Affandi and M. A. U. Absor, Electric field-induced anisotropic Rashba splitting in two dimensional tungsten dichalcogenides WX_2(X:S, Se, Te): A first-principles study, Physica E **114**, 113611 (2019).
[18] Q.-F. Yao, J. Cai, W.-Y. Tong, S.-J. Gong, J.-Q. Wang, X. Wan, C.-G. Duan, and J. H. Chu, Manipulation of the large Rashba spin splitting in polar two-dimensional transition-metal dichalcogenides, Phys. Rev. B **95**, 165401 (2017).
[19] S. Cho, W. Jung, J. Hong, B. Kim, G. Han, M. Leandersson, T. Balasubramanian, M. Arita, K. Shimada, J. H. Shim, C. Kim, and S. R. Park, Observation of Dresselhaus type spin splitting of zinc blende structure semiconductors by circular dichroic photoemission study, Current Appl. Phys. **30**, 96 (2021).
[20] W.-T. Wang, C. L. Wu, S. F. Tsay, M. H. Gau, I. Lo, H. F. Kao, D. J. Jang, J.-C. Chiang, M.-E. Lee, Y.-C. Chang, C.-N. Chen, and H. C. Hsueh, Dresselhaus effect in bulk wurtzite materials, Appl. Phys. Lett. **91**, 082110 (2007).
[21] S. Kuhlen, K. Schmalbuch, M. Hagedorn, P. Schlammes, M. Patt, M. Lepsa, G. Güntherodt, and B. Beschoten, Electric field-driven coherent spin reorientation of optically generated electron spin packets in InGaAs, Phys. Rev. Lett. **109**, 146603 (2012).
[22] R. Xie, P. Cao, Z. Xu, B. Xu, J. Fu, X. Zhu, X. Fu, S.-Y. Xie, Y. Jiang, and A. Pan, Three-dimensional Rashba spin splitting dominated by out-of-plane spin polarization, Phys. Rev. B **107**, 155436 (2023).
[23] M. A. U. Absor and F. Ishii, Intrinsic persistent spin helix state in two-dimensional group-iv monochalcogenide MX monolayers (M = Sn or Ge and X = S, Se, or Te), Phys. Rev. B **100**, 115104 (2019).
[24] S. A. Sasmito, M. Anshory, I. Jihad, and M. A. U. Absor, Reversible spin textures with giant spin splitting in two-dimensional GaXY (X = Se, Te; Y = Cl, Br, I) compounds for a persistent spin helix, Phys. Rev. B **104**, 115145 (2021).
[25] M. A. U. Absor and I. Santoso, Reversible canted persistent spin textures in two-dimensional ferroelectric bilayer WTe_2, J. Appl. Phys. **132**, 183906 (2022).
[26] M. A. U. Absor, Y. Faishal, M. Anshory, I. Santoso, and F. Ishii, Highly persistent spin textures with giant tunable spin splitting in the two-dimensional germanium monochalcogenides, J. Phys.: Condens. Matter **33**, 305501 (2021).
[27] M. Wang, J. Zhou, X. Xu, T. Zhang, Z. Zhu, Z. Guo, Y. Deng, M. Yang, K. Meng, B. He, J. Li, G. Yu, T. Zhu, A. Li, X. Han, and Y. Jiang, Field-free spin-orbit torque switching via out-of-plane spin-polarization induced by an antiferromagnetic insulator/heavy metal interface, Nat. Commun. **14**, 2871 (2023).
[28] P. Song, C.-H. Hsu, G. Vignale, M. Zhao, J. Liu, Y. Deng, W. Fu, Y. Liu, Y. Zhang, H. Lin, V. M. Pereira, and K. P. Loh, Coexistence of large conventional and planar spin Hall effect with long spin diffusion length in a low-symmetry semimetal at room temperature, Nat. Mater. **19**, 292 (2020).
[29] M.-W. Yoo, J. Tornos, A. Sander, L.-F. Lin, N. Mohanta, A. Peralta, D. Sanchez-Manzano, F. Gallego, D. Haskel, J. W. Freeland, D. J. Keavney, Y. Choi, J. Strempfer, X. Wang, M. Cabero, H. B. Vasili, M. Valvidares, G. Sanchez-Santolino, J. M. Gonzalez-Calbet, A. Rivera *et al.*, Large intrinsic anomalous Hall effect in $SrIrO_3$ induced by magnetic proximity effect, Nat. Commun. **12**, 3283 (2021).
[30] L. L. Tao and E. Y. Tsymbal, Spin-orbit dependence of anisotropic current-induced spin polarization, Phys. Rev. B **104**, 085438 (2021).
[31] M. Trushin and J. Schliemann, Anisotropic current-induced spin accumulation in the two-dimensional electron gas with spin-orbit coupling, Phys. Rev. B **75**, 155323 (2007).
[32] V. Edelstein, Spin polarization of conduction electrons induced by electric current in two-dimensional asymmetric electron systems, Solid State Commun. **73**, 233 (1990).
[33] J. C. R. Sánchez, L. Vila, G. Desfonds, S. Gambarelli, J. P. Attané, J. M. De Teresa, C. Magén, and A. Fert, Spin-to-charge conversion using Rashba coupling at the interface between non-magnetic materials, Nat. Commun. **4**, 2944 (2013).

[34] M. Isasa, M. C. Martínez-Velarte, E. Villamor, C. Magén, L. Morellón, J. M. De Teresa, M. R. Ibarra, G. Vignale, E. V. Chulkov, E. E. Krasovskii, L. E. Hueso, and F. Casanova, Origin of inverse Rashba-Edelstein effect detected at the Cu/Bi interface using lateral spin valves, Phys. Rev. B **93**, 014420 (2016).

[35] H.-Y. Yang, C. Huang, H. Ochoa, and M. A. Cazalilla, Extrinsic spin Hall effect from anisotropic Rashba spin-orbit coupling in graphene, Phys. Rev. B **93**, 085418 (2016).

[36] S. D. Ganichev and W. Prettl, Spin photocurrents in quantum wells, J. Phys.: Condens. Matter **15**, R935 (2003).

[37] S. Giglberger, L. E. Golub, V. V. Bel'kov, S. N. Danilov, D. Schuh, C. Gerl, F. Rohlfing, J. Stahl, W. Wegscheider, D. Weiss, W. Prettl, and S. D. Ganichev, Rashba and Dresselhaus spin splittings in semiconductor quantum wells measured by spin photocurrents, Phys. Rev. B **75**, 035327 (2007).

[38] E. Simon, A. Szilva, B. Ujfalussy, B. Lazarovits, G. Zarand, and L. Szunyogh, Anisotropic Rashba splitting of surface states from the admixture of bulk states: Relativistic *ab initio* calculations and $k \cdot p$ perturbation theory, Phys. Rev. B **81**, 235438 (2010).

[39] K. Miyamoto, A. Kimura, T. Okuda, K. Shimada, H. Iwasawa, H. Hayashi, H. Namatame, M. Taniguchi, and M. Donath, Massless or heavy due to two-fold symmetry: Surface-state electrons at W(110), Phys. Rev. B **86**, 161411(R) (2012).

[40] R. Friedrich, V. Caciuc, B. Zimmermann, G. Bihlmayer, N. Atodiresei, and S. Blügel, Creating anisotropic spin-split surface states in momentum space by molecular adsorption, Phys. Rev. B **96**, 085403 (2017).

[41] M. A. U. Absor, F. Ishii, H. Kotaka, and M. Saito, Spin-split bands of metallic hydrogenated ZnO (10-10) surface: First-principles study, AIP Adv. **6**, 025309 (2016).

[42] Z. S. Popović, J. M. Kurdestany, and S. Satpathy, Electronic structure and anisotropic Rashba spin-orbit coupling in monolayer black phosphorus, Phys. Rev. B **92**, 035135 (2015).

[43] S. Chakraborty and S. Raj, Anisotropic Rashba effect in two-dimensional non-Janus transition-metal dichalcogenide, mSSe(M = Mo, W) alloys, Phys. Rev. B **107**, 035420 (2023).

[44] S.-H. Zhang and B.-G. Liu, Anisotropic Rashba effect and charge and spin currents in monolayer BiTeI by controlling symmetry, Phys. Rev. B **100**, 165429 (2019).

[45] P. A. L. Sino, L.-Y. Feng, R. A. B. Villaos, H. N. Cruzado, Z.-Q. Huang, C.-H. Hsu, and F.-C. Chuang, Anisotropic Rashba splitting in Pt-based Janus monolayers PtXY (X,Y = S, Se, or Te), Nanoscale Adv. **3**, 6608 (2021).

[46] T. Hu, F. Jia, G. Zhao, J. Wu, A. Stroppa, and W. Ren, Intrinsic and anisotropic Rashba spin splitting in Janus transition-metal dichalcogenide monolayers, Phys. Rev. B **97**, 235404 (2018).

[47] M. Guillopé and B. Legrand, (110) surface stability in noble metals, Surf. Sci. **215**, 577 (1989).

[48] H. A. Zakaryan, A. G. Kvashnin, and A. R. Oganov, Stable reconstruction of the (110) surface and its role in pseudocapacitance of rutile-like RuO_2, Sci. Rep. **7**, 10357 (2017).

[49] A. Castellanos-Gomez, X. Duan, Z. Fei, H. R. Gutierrez, Y. Huang, X. Huang, J. Quereda, Q. Qian, E. Sutter, and P. Sutter, Van der waals heterostructures, Nat. Rev. Methods Primers **2**, 58 (2022).

[50] S. Gupta and B. I. Yakobson, What dictates Rashba splitting in 2D Van der waals heterobilayers, J. Am. Chem. Soc. **143**, 3503 (2021).

[51] A. Rezavand, N. Ghobadi, and B. Behnamghader, Electronic and spintronic properties of Janus $MSi_2P_xAs_y$ (M = Mo, W) monolayers, Phys. Rev. B **106**, 035417 (2022).

[52] M. Yagmurcukardes, Y. Qin, S. Ozen, M. Sayyad, F. M. Peeters, S. Tongay, and H. Sahin, Quantum properties and applications of 2D Janus crystals and their superlattices, Appl. Phys. Rev. **7**, 011311 (2020).

[53] S. Lee and Y.-K. Kwon, Unveiling giant hidden Rashba effects in two-dimensional Si_2Bi_2, npj 2D Mater. Appl. **4**, 45 (2020).

[54] B. Özdamar, G. Özbal, M. N. Çınar, K. Sevim, G. Kurt, B. Kaya, and H. Sevinçli, Structural, vibrational, and electronic properties of single-layer hexagonal crystals of group IV and V elements, Phys. Rev. B **98**, 045431 (2018).

[55] A. Bafekry, M. Yagmurcukardes, B. Akgenc, M. Ghergherehchi, and B. Mortazavi, First-principles investigation of electronic, mechanical and thermoelectric properties of graphene-like XBi (X = Si, Ge, Sn) monolayers, Phys. Chem. Chem. Phys. **23**, 12471 (2021).

[56] A. Bafekry, F. Shojai, D. M. Hoat, M. Shahrokhi, M. Ghergherehchi, and C. Nguyen, The mechanical, electronic, optical and thermoelectric properties of two-dimensional honeycomb-like of XSb (X = Si, Ge, Sn) monolayers: A first-principles calculations, RSC Adv. **10**, 30398 (2020).

[57] C. Barreteau, B. Michon, C. Besnard, and E. Giannini, High-pressure melt growth and transport properties of SiP, SiAs, GeP, and GeAs 2D layered semiconductors, J. Cryst. Growth **443**, 75 (2016).

[58] M. A. U. Absor, A. Lukmantoro, and I. Santoso, Full-zone persistent spin textures with giant spin splitting in two-dimensional group IV-V compounds, J. Phys.: Condens. Matter **34**, 445501 (2022).

[59] N. Troullier and J. L. Martins, Efficient pseudopotentials for plane-wave calculations, Phys. Rev. B **43**, 1993 (1991).

[60] T. Ozaki, H. Kino, J. Yu, M. J. Han, N. Kobayashi, M. Ohfuti, F. Ishii, T. Ohwaki, H. Weng, and K. Terakura, http://www.openmx-square.org/ (2009).

[61] T. Ozaki, Variationally optimized atomic orbitals for large-scale electronic structures, Phys. Rev. B **67**, 155108 (2003).

[62] T. Ozaki and H. Kino, Efficient projector expansion for the ab initio LCAO method, Phys. Rev. B **72**, 045121 (2005).

[63] J. P. Perdew, K. Burke, and M. Ernzerhof, Generalized gradient approximation made simple, Phys. Rev. Lett. **77**, 3865 (1996).

[64] W. Kohn and L. J. Sham, Self-consistent equations including exchange and correlation effects, Phys. Rev. **140**, A1133 (1965).

[65] T. Ozaki and H. Kino, Numerical atomic basis orbitals from H to Kr, Phys. Rev. B **69**, 195113 (2004).

[66] T. Tadano and S. Tsuneyuki, Self-consistent phonon calculations of lattice dynamical properties in cubic $SrTiO_3$ with first-principles anharmonic force constants, Phys. Rev. B **92**, 054301 (2015).

[67] H. Kotaka, F. Ishii, and M. Saito, Rashba effect on the structure of the bi one-bilayer film: Fully relativistic first-principles calculation, Jpn. J. Appl. Phys. **52**, 035204 (2013).

[68] H. Nitta, T. Yonezawa, A. Fleurence, Y. Yamada-Takamura, and T. Ozaki, First-principles study on the stability and electronic structure of monolayer GaSe with trigonal-antiprismatic structure, Phys. Rev. B **102**, 235407 (2020).

[69] Z. Y. Zhu, Y. C. Cheng, and U. Schwingenschlögl, Giant spin-orbit-induced spin splitting in two-dimensional

transition-metal dichalcogenide semiconductors, Phys. Rev. B **84**, 153402 (2011).

[70] See Supplemental Material at http://link.aps.org/supplemental/10.1103/PhysRevMaterials.7.104005 for phonon dispersion bands, symmetry-adapted SOC Hamiltonian, formation energy of Janus $SiBSi_2Bi$ with surface imperfection, and electric field-dependent of the Rashba parameters and Rashba precession for SFETs.

[71] S. Datta and B. Das, Electronic analog of the electro-optic modulator, Appl. Phys. Lett. **56**, 665 (1990).

[72] K. Yaji, Y. Ohtsubo, S. Hatta, H. Okuyama, K. Miyamoto, T. Okuda, A. Kimura, H. Namatame, M. Taniguchi, and T. Aruga, Large Rashba spin splitting of a metallic surface-state band on a semiconductor surface, Nat. Commun. **1**, 17 (2010).

[73] M. I. Dyakonov and V. I. Perel, Spin relaxation of conduction electrons in noncentrosymmetric semiconductors, Sov. Phys. Solid State **13**, 3023 (1972).

[74] R. Winkler, S. Papadakis, E. De Poortere, and M. Shayegan, *Spin-Orbit Coupling in Two-Dimensional Electron and Hole Systems* (Springer, Berlin, 2003).

[75] S. Vajna, E. Simon, A. Szilva, K. Palotas, B. Ujfalussy, and L. Szunyogh, Higher-order contributions to the Rashba-Bychkov effect with application to the Bi/Ag(111) surface alloy, Phys. Rev. B **85**, 075404 (2012).

[76] V. V. Volobuev, P. S. Mandal, M. Galicka, O. Caha, J. Sánchez-Barriga, D. Di Sante, A. Varykhalov, A. Khiar, S. Picozzi, G. Bauer, P. Kacman, R. Buczko, O. Rader, and G. Springholz, Giant Rashba splitting in $Pb_{1-x}Sn_xTe$ (111) topological crystalline insulator films controlled by Bi doping in the bulk, Adv. Mater. **29**, 1604185 (2017).

[77] M. Anshory and M. A. U. Absor, Strain-controlled spin-splitting in the persistent spin helix state of two-dimensional SnSe monolayer, Phys. E **124**, 114372 (2020).

[78] R. Arras, J. Gosteau, H. J. Zhao, C. Paillard, Y. Yang, and L. Bellaiche, Rashba-like spin-orbit and strain effects in tetragonal $PbTiO_3$, Phys. Rev. B **100**, 174415 (2019).

[79] J. Zhang, S. Jia, I. Kholmanov, L. Dong, D. Er, W. Chen, H. Guo, Z. Jin, V. B. Shenoy, L. Shi, and J. Lou, Janus monolayer transition-metal dichalcogenides, ACS Nano **11**, 8192 (2017).

[80] R. Sant, M. Gay, A. Marty, S. Lisi, R. Harrabi, C. Vergnaud, M. T. Dau, X. Weng, J. Coraux, N. Gauthier, O. Renault, G. Renaud, and M. Jamet, Synthesis of epitaxial monolayer Janus SPtSe, npj 2D Mater. Appl. **4**, 41 (2020).

[81] A.-Y. Lu, H. Zhu, J. Xiao, C.-P. Chuu, Y. Han, M.-H. Chiu, C.-C. Cheng, C.-W. Yang, K.-H. Wei, Y. Yang, Y. Wang, D. Sokaras, D. Nordlund, P. Yang, D. A. Muller, M.-Y. Chou, X. Zhang, and L.-J. Li, Janus monolayers of transition metal dichalcogenides, Nat. Nanotechnol. **12**, 744 (2017).

[82] Y.-C. Lin, C. Liu, Y. Yu, E. Zarkadoula, M. Yoon, A. A. Puretzky, L. Liang, X. Kong, Y. Gu, A. Strasser, H. M. Meyer III, M. Lorenz, M. F. Chisholm, I. N. Ivanov, C. M. Rouleau, G. Duscher, K. Xiao, and D. B. Geohegan, Low energy implantation into transition-metal dichalcogenide monolayers to form Janus structures, ACS Nano **14**, 3896 (2020).

[83] Y. Qin, M. Sayyad, A. R.-P. Montblanch, M. S. G. Feuer, D. Dey, M. Blei, R. Sailus, D. M. Kara, Y. Shen, S. Yang, A. S. Botana, M. Atature, and S. Tongay, Reaching the excitonic limit in 2D Janus monolayers by *in situ* deterministic growth, Adv. Mater. **34**, 2106222 (2022).

[84] C. W. Jang, W. J. Lee, J. K. Kim, S. M. Park, S. Kim, and S.-H. Choi, Growth of two-dimensional Janus MoSSe by a single *in situ* process without initial or follow-up treatments, NPG Asia Mater. **14**, 15 (2022).

[85] J. Gou, L. Kong, X. He, Y. L. Huang, J. Sun, S. Meng, K. Wu, L. Chen, and A. T. S. Wee, The effect of moiré superstructures on topological edge states in twisted bismuthene homojunctions, Sci. Adv. **6**, eaba2773 (2020).

[86] X. Wu, Y. Shao, H. Liu, Z. Feng, Y.-L. Wang, J.-T. Sun, C. Liu, J.-O. Wang, Z.-L. Liu, S.-Y. Zhu, Y.-Q. Wang, S.-X. Du, Y.-G. Shi, K. Ibrahim, and H.-J. Gao, Epitaxial growth and air-stability of monolayer antimonene on $PdTe_2$, Adv. Mater. **29**, 1605407 (2017).

[87] M. Aras and Ç. Kılıç, Electrical tuning of spin splitting in Bi-doped ZnO nanowires, Phys. Rev. B **97**, 035405 (2018).

[88] K. Wu, J. Chen, H. Ma, L. Wan, W. Hu, and J. Yang, Two-dimensional giant tunable Rashba semiconductors with two-atom-thick buckled honeycomb structure, Nano Lett. **21**, 740 (2021).

[89] J. Chen, K. Wu, W. Hu, and J. Yang, Tunable Rashba spin splitting in two-dimensional polar perovskites, J. Phys. Chem. Lett. **12**, 1932 (2021).

[90] Y. Jin, J. Li, G. Wang, Q. Zhang, Z. Liu, and X. Mao, Giant tunable Rashba spin splitting in two-dimensional polar perovskites $TlSnX_3$ (X = Cl, Br, I), Phys. Chem. Chem. Phys. **24**, 17561 (2022).

[91] K. Takase, Y. Ashikawa, G. Zhang, K. Tateno, and S. Sasaki, Highly gate-tuneable Rashba spin-orbit interaction in a gate-all-around InAs nanowire metal-oxide-semiconductor field-effect transistor, Sci. Rep. **7**, 930 (2017).

[92] P. Chuang, S.-C. Ho, L. W. Smith, F. Sfigakis, M. Pepper, C.-H. Chen, J.-C. Fan, J. P. Griffiths, I. Farrer, H. E. Beere, G. A. C. Jones, D. A. Ritchie, and T.-M. Chen, All-electric all-semiconductor spin field-effect transistors, Nat. Nanotechnol. **10**, 35 (2015).

[93] F. Trier, D. C. Vaz, P. Bruneel, P. Noël, A. Fert, L. Vila, J.-P. Attané, A. Barthélémy, M. Gabay, H. Jaffrès, and M. Bibes, Electric-field control of spin current generation and detection in ferromagnet-free $SrTiO_2$-based nanodevices, Nano Lett. **20**, 395 (2020).

[94] J.-H. Lin, H. Zhang, X.-L. Cheng, and Y. Miyamoto, Single-layer group IV-V and group V-IV-III-VI semiconductors: Structural stability, electronic structures, optical properties, and photocatalysis, Phys. Rev. B **96**, 035438 (2017).

[95] M. N. Çınar, G. O. Sargın, K. Sevim, B. Özdamar, G. Kurt, and H. Sevinçli, Ballistic thermoelectric transport properties of two-dimensional group III-VI monolayers, Phys. Rev. B **103**, 165422 (2021).

[96] T. V. Vu, V. T. T. Vi, H. V. Phuc, A. I. Kartamyshev, and N. N. Hieu, Oxygenation of Janus group III monochalcogenides: First-principles insights into $GaInXO$ (X = S, Se, Te) monolayers, Phys. Rev. B **104**, 115410 (2021).